

PHYSICS

Observation of symmetry-protected topological band with ultracold fermions

Bo Song,^{1*} Long Zhang,^{2,3*} Chengdong He,^{1*} Ting Fung Jeffrey Poon,^{2,3} Elnur Hajiyev,¹ Shanchao Zhang,¹ Xiong-Jun Liu,^{2,3,4†} Gyu-Boong Jo^{1†}

Symmetry plays a fundamental role in understanding complex quantum matter, particularly in classifying topological quantum phases, which have attracted great interests in the recent decade. An outstanding example is the time-reversal invariant topological insulator, a symmetry-protected topological (SPT) phase in the symplectic class of the Altland-Zirnbauer classification. We report the observation for ultracold atoms of a noninteracting SPT band in a one-dimensional optical lattice and study quench dynamics between topologically distinct regimes. The observed SPT band can be protected by a magnetic group and a nonlocal chiral symmetry, with the band topology being measured via Bloch states at symmetric momenta. The topology also resides in far-from-equilibrium spin dynamics, which are predicted and observed in experiment to exhibit qualitatively distinct behaviors in quenching to trivial and nontrivial regimes, revealing two fundamental types of spin-relaxation dynamics related to bulk topology. This work opens the way to expanding the scope of SPT physics with ultracold atoms and studying nonequilibrium quantum dynamics in these exotic systems.

INTRODUCTION

The discovery of the quantum Hall effect in a two-dimensional (2D) electron gas (1, 2) brought about a new fundamental concept, topological quantum phase, whose characterization is beyond Landau symmetry-breaking theory, to condensed-matter physics (3). Recent extensive studies have generated two broad categories of topological matter, the topologically ordered phases (4–6) and symmetry-protected topological (SPT) phases (7–10), which exhibit long- and short-range quantum entanglement, respectively. Unlike topological orders, which are robust against any local perturbations, an SPT phase with a bulk gap has gapless or degenerate boundary modes that are only robust against local perturbations, respecting the given symmetries. The earliest examples of SPT phases include the 1D Su-Schrieffer-Heeger (SSH) model for fermions (11) and the spin-1 antiferromagnetic chain for bosons (12). The search for new SPT phases has been greatly revived in the recent decade due to the groundbreaking discovery of time-reversal invariant topological insulators in 2D and 3D materials, which exhibit symmetry-protected helical edge or surface modes at the boundary and are characterized by a \mathbb{Z}_2 invariant (13, 14). Topological insulators also inspired generalizations to SPT phases arising from spatial symmetries, in unconventional superconductors and superfluids (15).

Despite the broad classes of SPT phases predicted in theory, only a small portion of these phases have been observed in the experiments. In comparison with solid-state materials, ultracold atoms are extremely clean systems, which can provide controllable platforms in exploring new SPT phases, with many theoretical schemes having been proposed (16–18). To date, some of the novel topological features of the SSH model have been probed in experiments with ultracold bosons (19–21), whereas the realization of the SPT phase, which can only exist for fermions in the noninteracting limit, has not been reported. Here, we propose and

realize, for the first time, a 1D optical Raman lattice of fermions, which hosts a new SPT phase that is beyond particle-hole or chiral symmetry protection, as usually required in Altland-Zirnbauer (AZ) classification of 1D states (15, 22). We measure the topology via Bloch states at symmetric momenta (23), and the quench dynamics and unveil two fundamental types of spin-relaxation mechanisms related to band topology in this SPT system.

RESULTS AND DISCUSSION

SPT phases

We start with the Hamiltonian for spin-1/2 ultracold fermions trapped in a 1D optical Raman lattice potential (Fig. 1A), whose realization in experiment will be presented later

$$H = \left[\frac{p_x^2}{2m} + \frac{V_{\uparrow}^{\text{latt}}(x) + V_{\downarrow}^{\text{latt}}(x)}{2} \right] \otimes \hat{\mathbf{1}} + \left[\frac{\delta}{2} + \frac{V_{\uparrow}^{\text{latt}}(x) - V_{\downarrow}^{\text{latt}}(x)}{2} \right] \sigma_z + \mathcal{M}(x) \sigma_x \quad (1)$$

where $p_x^2/2m$ is the kinetic energy for motion in the x direction, $\hat{\mathbf{1}}$ is a two-by-two unit matrix, $\sigma_{x,y,z}$ are Pauli matrices in spin space, $V_{\uparrow,\downarrow}^{\text{latt}}(x) = V_{\uparrow,\downarrow} \cos^2(k_0 x)$ denote the 1D optical lattice potentials for spin $|\uparrow, \downarrow\rangle$ states, with $V_{\uparrow,\downarrow}$ being the lattice depths and $k_0 = \pi/a$ (a is the lattice constant), the Raman lattice potential $\mathcal{M}(x) = M_0 \cos(k_0 x)$ with amplitude M_0 , and δ is the two-photon detuning of Raman coupling.

The Hamiltonian (Eq. 1) supports novel topological phases protected by symmetries. With the lattice potential $V_{\uparrow,\downarrow}^{\text{latt}}(x)$, the spin-conserved hopping ($t_{\uparrow,\downarrow}$) is induced, whereas the Raman potential $\mathcal{M}(x)$ accounts for the hopping (t_{so}) that flips the atomic spin (Fig. 1A). The Bloch Hamiltonian for the lowest s -band physics can be obtained by $\mathcal{H}(\vec{m}) = -2t_0 \cos q_x a \sigma_z + 2t_{\text{so}} \sin q_x a \sigma_y + \vec{m} \cdot \vec{\sigma} + 2t_1 \cos q_x a \hat{\mathbf{1}}$ (see the Supplementary Materials), where we take $\vec{m} = (m_x m_y m_z)$ for a generic study, q_x as the Bloch quasi-momentum, and the hopping coefficients $t_{0/1} = (t_{\uparrow} \pm t_{\downarrow})/2$. The Hamiltonian \mathcal{H} with $m_x = 0$ exhibits a chiral symmetry defined by $\sigma_x \mathcal{H} \sigma_x = -\mathcal{H}$ if the lattice is spin-independent $V_{\uparrow}^{\text{latt}} = V_{\downarrow}^{\text{latt}}$,

Copyright © 2018
The Authors, some
rights reserved;
exclusive licensee
American Association
for the Advancement
of Science. No claim to
original U.S. Government
Works. Distributed
under a Creative
Commons Attribution
NonCommercial
License 4.0 (CC BY-NC).

¹Department of Physics, The Hong Kong University of Science and Technology, Clear Water Bay, Kowloon, Hong Kong, China. ²International Center for Quantum Materials, School of Physics, Peking University, Beijing, China. ³Collaborative Innovation Center of Quantum Matter, Beijing 100871, China. ⁴Synergetic Innovation Center for Quantum Effects and Applications, Hunan Normal University, Changsha 410081, China.

*These authors contributed equally to this work.

†Corresponding author. Email: xiongjunliu@pku.edu.cn (X.-J.L.); gbj@ust.hk (G.-B.J.)

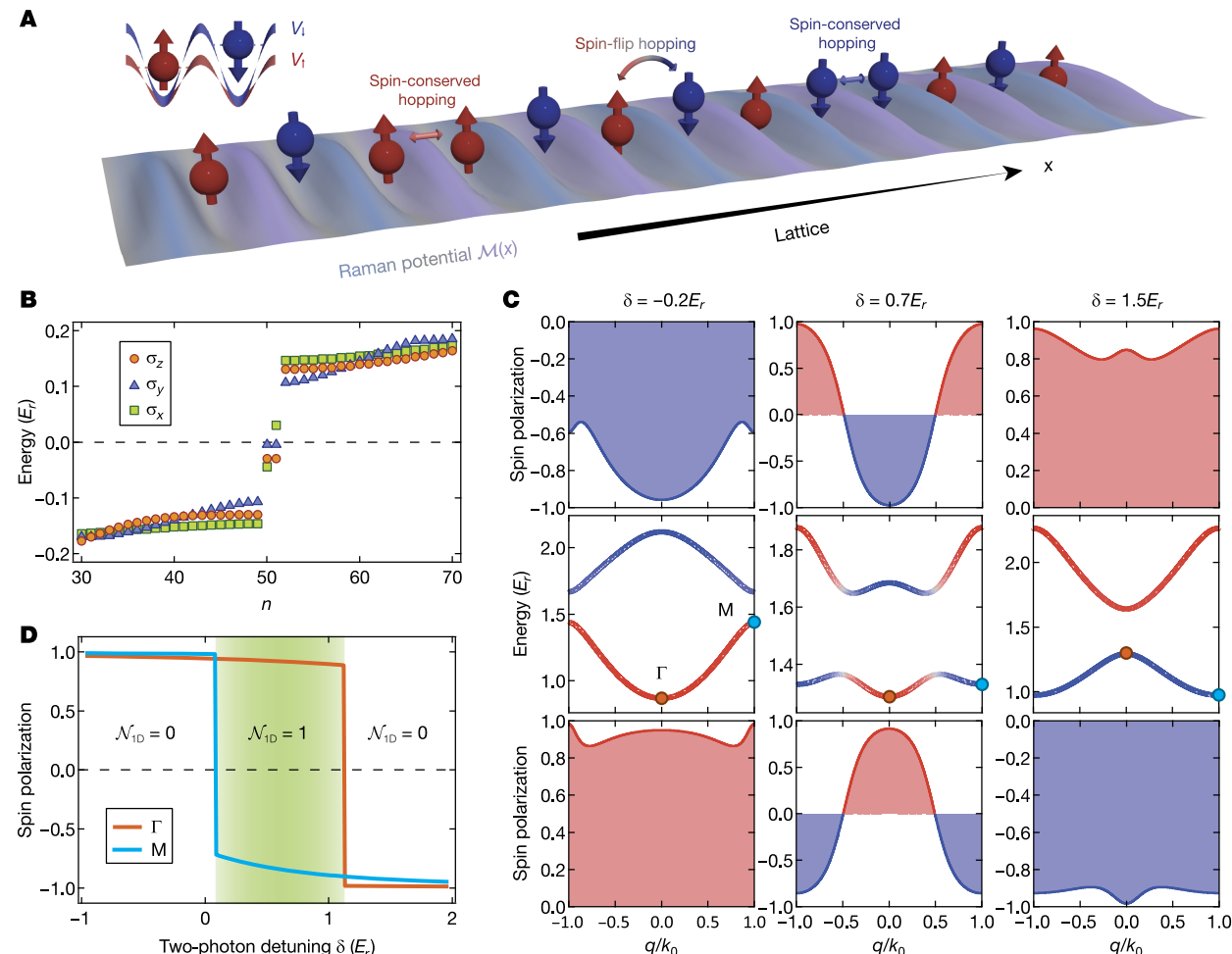


Fig. 1. SPT phases and band topology. (A) Sketch of the 1D Raman lattice model. A spin-dependent lattice potential induces spin-conserved hopping, whereas the Raman potential contributes to spin-flip hopping. (B) Bulk and boundary energy spectra obtained by full-band diagonalization with a Zeeman perturbation field of strength $0.1E_r$ and along the z (σ_z , orange circles), y (σ_y , blue triangles), and x (σ_x , green squares) direction, respectively. The in-gap states are boundary modes. The parameters are taken as $V_\downarrow = 5E_r$, and $M_0 = 1.0E_r$ [the same for (C) and (D)]. (C) Band structure (the second row) and spin textures of both the lowest band (the third row) and the second band (the first row) for $\delta = -0.2E_r$ (left), $\delta = 0.7E_r$ (middle), and $\delta = 1.5E_r$ (right), respectively. (D) The spin polarizations at Γ and M points of the lowest band determine the topological trivial ($v = 0$) and nontrivial ($v = 1$) regimes.

which gives $t_\uparrow = t_\downarrow$, and belongs to the AIII class according to the AZ classification (16, 22). The topology of this AIII class phase is quantified by an integer winding number (\mathbb{Z}) in the single-particle regime, pictorially characterized by the circles that the spin of Bloch states winds over the first Brillouin zone (FBZ), and determines the number of midgap end states due to bulk-boundary correspondence. Furthermore, in the interacting regime, it was shown that the topology of the 1D AIII class topological insulator is reduced from \mathbb{Z} to \mathbb{Z}_4 (16), which is closely related to the Fidkowski-Kitaev \mathbb{Z}_8 classification of 1D interacting Majorana chains of the BDI (chiral orthogonal) class (24).

The striking result is that a new topological phase can be achieved beyond the chiral symmetry protection when the lattice depths $V_{\uparrow\downarrow}^{\text{latt}}$ and $t_{\uparrow\downarrow}$ are spin-dependent, in which the regime with no chiral symmetry preserves and the bulk energy spectrum is asymmetric. From the numerical results in Fig. 1B, one finds that the midgap and degenerate end states are obtained for $\vec{m} = m_y \hat{e}_y$ and $\vec{m} = m_z \hat{e}_z$, respectively, whereas only a nonzero m_x term splits out the degeneracy. The existence of midgap or degenerate end states manifests new SPT phases, as shown below. We first consider the case with $\vec{m} = 0$. One can verify that $\mathcal{H}(\vec{m} = 0)$ satisfies

a magnetic group symmetry defined as the product of time-reversal and mirror symmetries (see the Supplementary Materials), giving $M_x = \sigma_z K \otimes R_x$ with $M_x \mathcal{H}(q_x) M_x^{-1} = \mathcal{H}(-q_x)$, where K is the complex conjugate, and R_x denotes the spatial reflection along the x axis. Besides, the Hamiltonian also satisfies a nonlocal chiral symmetry defined as $S = \sigma_z \otimes T_x(k_0) \otimes R_x$, where $T_x(k_0)$ is a k_0 -momentum translation, yielding $S \mathcal{H}(q_x) S^{-1} = -\mathcal{H}(q_x)$. The midgap end states at left-hand ($|\psi_L\rangle$) and right-hand ($|\psi_R\rangle$) boundaries are protected by the both symmetries under a novel mechanism. First, by definition, both M_x and S transform one of $|\psi_{L/R}\rangle$ to the other. Moreover, their commutation and anticommutation relations with \mathcal{H} imply that the magnetic group symmetry (nonlocal chiral symmetry) connects the two end states with identical (opposite) energy, which forces the two end states $|\psi_{L/R}\rangle$ to be of zero energy (that is, midgap states in the presence of both symmetries), which is the case for \vec{m} along the y axis. The m_z term keeps the M_x symmetry, hence protects the end-state degeneracy, with the degenerate end modes existing as long as the gap is not closed and is in the topological regime for $|m_z| < 2t_0$ (see the Supplementary Materials), whereas the m_x term breaks the M_x symmetry and splits out the degeneracy, leading to the

end-state spectra in Fig. 1B. Note that the identity matrix t_1 term in the Hamiltonian does not affect the spin winding of the Bloch states. Thus, the topological invariant of the present system is still characterized by an integer winding number \mathcal{N}_{1D} when the M_x symmetry preserves (without m_x term), whereas the nonlocal chiral symmetry S further protects the end states to be zero-energy modes. In the experiment, a nonzero m_z term can be easily engineered by manipulating the two-photon detuning δ of the Raman coupling. In this case, the magnetic group ensures that Bloch states at the two symmetric momenta $\{\Lambda_j\} = \{\Gamma(q_x = 0), M(q_x = \pi/a)\}$ are eigenstates of σ_z having the spin polarization $P(\Lambda_j) = \pm 1$. The winding number of the lowest band can be further obtained from a spin index through $\mathcal{N}_{1D} = v \cdot \text{sgn}[P(\Gamma)]$, with the spin index v being introduced as $(-1)^v = \prod_j \text{sgn}[P(\Lambda_j)]$, similar to the study of Liu *et al.* (23). The topologically nontrivial (trivial) phase corresponds to $v = 1(0)$. Figure 1C shows the spin texture with different parameter conditions, from which the \mathbb{Z}_2 index and then the winding number can be read out directly, and Fig. 1D presents the phase diagram versus δ .

Quench dynamics

We examine the spin dynamics after a quench from one phase to another. The quench is performed by suddenly ramping the two-photon detuning from δ_i to δ_f , with δ_i and δ_f corresponding to two topologically distinct regimes. The quantum dynamics are captured by the time-dependent density matrix $\rho(t)$, which satisfies the Lindblad master equation (25, 26)

$$\dot{\rho} = -\frac{i}{\hbar} [H' \rho] + \gamma \left(L \rho L^\dagger - \frac{1}{2} \{L^\dagger L, \rho\} \right) \quad (2)$$

where γ denotes the noise-induced decay rate, and L is the Lindblad operator characterizing the effects of the environment. For a real ultracold atom system, we consider an external trapping potential for the study and the Hamiltonian $H' = H + V_{\text{trap}}$, with $V_{\text{trap}}(x) = \frac{1}{2}m\omega_x^2x^2$ and ω_x being the trapping frequency. The sharp contrast between the topological and trivial phases, which we assume for this study to be away from the critical point of phase transition, is that the spin of the Bloch states in the FBZ winds over all directions in the y - z plane in the former case, whereas it is polarized to $+z$ (or $-z$) direction in the latter (Fig. 1C). This feature accounts for different fundamental mechanisms governing the quench spin dynamics, as given below.

We first consider the case without dissipation ($\gamma = 0$). In this regime, the time evolution is unitary, and the spin dynamics are governed by the following two-quantum processes, namely, the interband transition at each quasi-momentum q_x due to nonequilibrium population after the quench and the intraband transition induced by the trapping potential between Bloch states of different momenta. The numerical simulation of the spin dynamics at Γ and M points is shown in Fig. 2 (A and B) for a quench to topological ($\delta_f = 0.7E_r$) and trivial ($\delta_f = 2.0E_r$) phases, respectively. In both cases, the spin dynamics exhibit a fast oscillation due to interband transitions, with the oscillation frequency determined by the local band gap at Γ and M points. However, the spin dynamics for quench to topological phase also exhibit a slower spin wave-like collective oscillation associated with a fast decay in the very beginning stage, which is absent in the quench to trivial phase. This novel behavior is a consequence of the topological spin texture or spin-orbit fields in momentum space (see the Supplementary Materials). In the topological regime, the intraband transitions induced by trapping potential randomize the fast oscillation caused by interband transitions due to the strongly momentum-dependent spin-orbit fields, leading to a fast

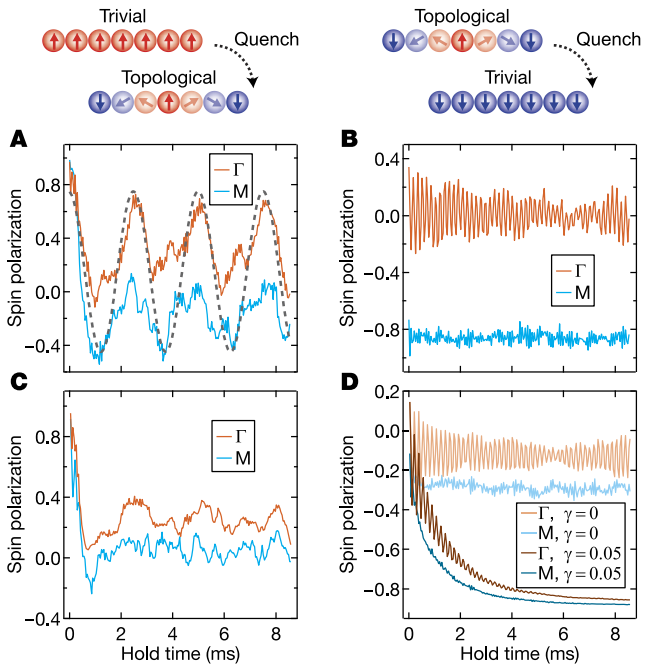


Fig. 2. Quench dynamics of SPT bands. The numerical simulation is performed in the half-filling condition (one atom per site) for quench process from trivial to topological regimes, with $\delta_i = -0.2E_r$ and $\delta_f = 0.7E_r$ in (A) and (C), and from topological to trivial regimes, with $\delta_i = 0.7E_r$ and $\delta_f = 2.0E_r$, in (B) and (D). In all the cases, the trapping frequency reads $\omega_x = (2\pi)300$ Hz, and the optical Raman lattice potentials $V_\uparrow = 2.5E_r$, $V_\downarrow = 5E_r$, and $M_0 = 1.0E_r$. For comparison, we plot the dashed line in (A) for an oscillation of frequency $\sqrt{\omega_x^2 + \Delta E^2}$, with $\Delta E = 0.07E_r$, characterizing a detuning of magnitude between the bandwidth and the energy difference of Γ and M points. (A and B) Quench dynamics for spin polarizations at Γ and M points at zero temperature and without dissipation. (C) Quench spin dynamics from the trivial to the topological regime at the temperature $T = 100$ nK, with the noise-induced dephasing rate $\gamma = 0.03$. (D) Quench spin dynamics from topological to trivial at $T = 100$ nK, with dissipation rate taken as $\gamma = 0$ and 0.05 , respectively.

decay in the very beginning and leaving only a collective oscillation governed by the trapping potential. Instead, in the trivial regime that is away from critical point, all the spin states and spin-orbit fields of FBZ approximately point to the $+z$ (or $-z$) direction. Thus, the trapping-induced intraband transitions have negligible effect on the spin oscillation.

We further show in Fig. 2 (C and D) the quench dynamics with dissipation, as captured by the nonunitary part of Eq. 2. For a quench to the trivial phase, because the spin dynamics are dominated by the interband oscillations, the dissipation mainly results from the decay of the excited bands. In comparison, for the quench to the topological phase, the dissipation mainly describes a spin dephasing of the collective oscillation induced by trapping. The Lindblad operator L then takes the form

$L = \sum_{m,n} L_{mn} |n\rangle\langle m|$ (for decay) and $L = \sum_n L_n |n\rangle\langle n|$ (for dephasing), respectively, and for qualitative modification of dynamical behaviors, the latter effect is typically much weaker than the former. Here, $|n\rangle$ denotes the eigenstates of the postquench Hamiltonian $H(\delta_f) + V_{\text{trap}}$. The numerical simulation shows that the quench dynamics from trivial to topological regime resemble the one without dissipation, except for a small decay in the amplitude of collective oscillation, followed by a quick interband balance in the very beginning (Fig. 2C), whereas the dynamics in the other way round render a pure decay from initial state to the final equilibrium phase (Fig. 2D). With these results, we draw the conclusion that

the trapping potential (dissipation) has dominant effects on the spin dynamics after the quench due to the topological (trivial) spin textures of the final SPT band, as observed in the present experiment.

Optical Raman lattices for ytterbium atoms

To realize the Hamiltonian (1) in the experiment, we use a 1D optical lattice dressed by a periodic Raman coupling potential, making up a so-called optical Raman lattice, as described in Fig. 3A (16, 27). The optical Raman lattice is generated by the use of the intercombination $\lambda_0 = 2\pi/k_0 = 556$ nm transition of ^{173}Yb atoms, blue-detuned by ~ 1 GHz from the $^1\text{S}_0(F = \frac{5}{2}) \leftrightarrow ^3\text{P}_1(F' = \frac{7}{2})$ transition. The lattice potential produced by counter-propagating lights, being linearly polarized along the z direction, forms a spin-dependent potential $V_{\sigma}^{\text{latt}}(x) = V_{\sigma} \cos^2(k_0 x)$,

$$\text{where } V_{\sigma=\{\uparrow,\downarrow\}} = \sum_{F'} \hbar \frac{|\Omega_{\sigma,F'}^{\text{latt}}|^2}{4\Delta_{F'}}, \text{ with } |\uparrow\rangle = |m_F = \frac{5}{2}\rangle \text{ and } |\downarrow\rangle = |m_F = \frac{3}{2}\rangle$$

(28). The effective Rabi frequencies $\Omega_{\sigma,F'}^{\text{latt}}$ and the single-photon detunings $\Delta_{F'}$ are determined from all relevant transitions to the excited $F' = (\frac{7}{2}, \frac{5}{2}, \frac{3}{2})$ states in the $^3\text{P}_1$ manifold (Fig. 3B). With the quantized axis set along the z direction, a standing-wave lattice light of frequency $\omega_0 = k_0 c$ (c is the speed of light), denoted as $E_{1x} \propto e_z 2\bar{E}_{1x} e^{-i\omega_0 t} \cos(k_0 x)$, where \bar{E}_{1x} is the amplitude of the light field and e_z is the unit vector in the z direction, induces a π transition between the ground and the excited states, thus resulting in the relation $V_{\downarrow}/V_{\uparrow} = 3.84$ (Fig. 3A).

Another circularly polarized light of frequency ω_1 , denoted as $E_{1z} \propto (e_x + ie_y)\bar{E}_{1z} e^{i(k_0 z - \omega_1 t)}$, is applied along the z direction and in-

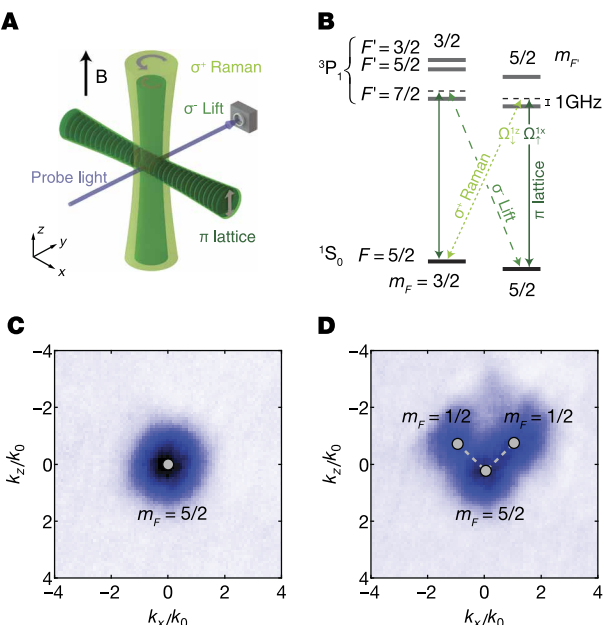


Fig. 3. A sketch of the experimental setup. (A) The experimental setup consists of a 1D optical lattice with lattice along the x direction and a perpendicular Raman beam generating a periodic Raman potential $\mathcal{M}(x) = M_0 \cos(k_0 x)$. A circularly polarized beam is added along the quantized axis in the z direction, introducing the spin-dependent ac Stark shift. (B) Both the lattice and the Raman beams are near blue-detuned from the $F = \frac{5}{2} \rightarrow F' = \frac{7}{2}$ intercombination transition and induce the Raman transition between the $|\uparrow\rangle = |\frac{5}{2}, \frac{5}{2}\rangle$ and $|\downarrow\rangle = |\frac{5}{2}, \frac{3}{2}\rangle$ hyperfine states of the $^1\text{S}_0$ ground manifold. (C) TOF image of $m_F = 5/2$ atoms without pulsing optical Raman lattice beams. The direction of the gravity is along the z direction. (D) When the optical Raman lattice is briefly switched on in such a way that the $m_F = 1/2$ atoms are coupled out, two $m_F = 1/2$ clouds are relatively shifted by $\sim 2k_0$ along the x direction.

duces the Raman coupling between $|\uparrow\rangle$ and $|\downarrow\rangle$ states with the Rabi frequency $\Omega_{\downarrow,F'}^{\text{latt}}$. Both the lattice and Raman lights are generated by a single laser source and controlled by phase-locked acousto-optical modulators, making the frequency difference $\delta\omega = \omega_0 - \omega_1$ tunable. The Raman coupling potential $\mathcal{M}(x, z)$ takes the form $\mathcal{M}(x, z) \propto M_0 e^{ik_0 z} (e^{ik_0 x} + e^{-ik_0 x})$, where $M_0 = \sum_{F'} \Omega_{\uparrow,F'}^{\text{latt}} \Omega_{\downarrow,F'}^{\text{latt}} / 2\Delta_{F'}$. Because we focus on the motion along the x direction, which is uncoupled to the other two directions, we neglect the irrelevant phase $e^{ik_0 z}$ and write the Raman potential as $\mathcal{M}(x) = M_0 \cos(k_0 x)$. To separate out spin-1/2 space from other hyperfine states of the ground manifold, an additional circularly polarized 556-nm light, $E_{2z} \propto (e_x - ie_y)\bar{E}_{2z} e^{ik_0 z}$ (called as a lift beam), is applied along the z direction to induce spin-dependent ac Stark shift (28). Note that the spin-dependent lattice potential $V_{\uparrow,\downarrow}^{\text{latt}}(x)$ adds an additional energy shift, δ_0 , to the Bloch bands corresponding to two spin states, which can be readily compensated by the two-photon detuning. Finally, a Zeeman term is given as $m_z = (\delta - \delta_0)/2$, where δ_0 is the on-site energy difference in the spin-dependent lattice.

Symmetry in an optical Raman lattice

To investigate a new SPT band in the experiment, it is crucial to test that the system has a mirror-symmetric optical Raman lattice and that a Zeeman term \vec{m} is parallel to the mirror plane, leading to a magnetic group symmetry. In the experiment, the two-photon detuning δ sets a nonzero m_z , but a finite m_x term may be generated when the Raman potential $\mathcal{M}(x)$ breaks a mirror symmetry of the lattice and thus induces on-site spin flipping (see the Supplementary Materials). When the Raman beam E_{1z} is not perfectly along the z direction with the wave vector $\hat{k} = k_0 e_z + k_{\perp,x} e_x + k_{\perp,y} e_y$, the Raman potential has an additional phase factor $\mathcal{M}(x) = M_0 \cos(k_0 x) e^{ik_{\perp,x} x}$, therefore breaking a mirror symmetry unless $k_{\perp,x}$ is close to zero.

We begin with spin-polarized $m_F = 5/2$ fermions (Fig. 3C), followed by a brief pulse of the optical Raman lattice beams, and then examine the wave number $k_{\perp,x}$ of the Raman beam E_{1z} . After the time-of-flight (TOF) expansion, as described in Fig. 3D, $m_F = 5/2$ atoms are shifted downward (in the $-\hat{z}$ direction), whereas the $m_F = 3/2$ atoms are shifted upward (in the $+\hat{z}$ direction), which manifests spin-orbit coupling induced by the Raman transition (28–34). However, along the x direction, $m_F = 3/2$ atoms absorb the momentum shift of $\pm 1/2\hbar k_0$, resulting to two small $m_F = 3/2$ clouds after TOF. In the experiment, we spin-orbit-couple multiple hyperfine states $m_F = 5/2, 3/2, 1/2$ in such a way that two small daughter clouds of $m_F = 1/2$ atoms are well separated from the $m_F = 5/2$ atoms. Finally, we assess the left-right symmetry of the atom diffraction and determine the angle θ between the lattice and the Raman beam to be $\theta = 89.3 \pm 1.5$ or the wave number $k_{\perp,x} = 0.01k_0$, which ensures negligible m_x term in the Hamiltonian (Eq. 1) and, therefore, a magnetic group symmetry.

Observation of the SPT band

We now observe an SPT band for ultracold fermions by loading an equal mixture of $|\uparrow\rangle$ and $|\downarrow\rangle$ atoms, prepared at $T/T_F = 0.4$ in a crossed optical dipole trap (ODT), where T_F is the Fermi temperature of the system (28), into the optical Raman lattice. An optical ac Stark shift, separating out an effective spin-1/2 subspace from other hyperfine levels, is applied within 5 ms before the optical lattice potential, and the Raman dressing beams are adiabatically switched on with a 10-ms exponential ramp to the final value. During the ramp, the crossed ODT power is increased to compensate the antitrapping effect arising from the blue-detuned Raman potential. Consequently, the temperature is increased to $T = 125(20)$ nK when all optical potentials with $V_{\uparrow}(V_{\downarrow}) = 1.1E_r$

($4.2E_r$) and Raman coupling $M_0 = 1.88 E_r$, where $E_r = \hbar^2 k_0^2 / 2m$ and m is the mass of an ytterbium atom, are turned on. In the experiment, the spin-resolved TOF imaging is taken after all the laser beams are suddenly switched off, followed by spin-sensitive blast lights (28).

The crucial feature of SPT bands is the nontrivial spin texture within the FBZ. Figure 4A shows measured spin textures $P(q_x) = (n_\uparrow(q_x) - n_\downarrow(q_x)) / (n_\uparrow(q_x) + n_\downarrow(q_x))$ within the FBZ reconstructed from the integrated momentum distribution along the \hat{x} direction for different values of the two-photon detuning. Because the two-photon detuning δ is scanned from the negative to positive value, the overall spin polarization of the lowest s -band gradually changes from $|\uparrow\rangle$ (red) to $|\downarrow\rangle$ (blue). However, when the Raman transition resonantly couples the two lowest s -bands corresponding to $|\uparrow\rangle$ and $|\downarrow\rangle$, respectively, the spin polarization changes from one to the other within the FBZ, as shown in Fig. 4B. Figure 4C also visualizes the coexistence of different spin domains within the FBZ in the topological regime. Finally, we use the connection between the spin index and the $P(\Gamma, M)$ and determine $(-1)^v = \prod_{i=\Gamma, M} \text{sgn}[P(\Lambda_i)]$ by measuring the averaged spin polarization $P(\Lambda_i) =$

$\frac{1}{10} \int_{\Lambda_i - 0.05k_r}^{\Lambda_i + 0.05k_r} P(q') dq'$ that takes into account the optical resolution of the imaging system (23). Figure 4D shows the emergence of SPT bands ($v = 1$) out of trivial bands ($v = 0$). The spin-dependent lattice shifts the topological regime due to the on-site energy difference, and furthermore, the finite temperature effect reduces the topological regime, in good agreement with the prediction (indicated by shaded region in Fig. 4D).

Adiabatic control of the band topology

In a second set of experiments, we demonstrate the adiabatic preparation of the topological band starting from the trivial regime and vice versa. In the experiment, a topological band is adiabatically prepared at $\delta = 0.8(3)E_r$, as described in the previous experiment, and subsequently, the two-photon detuning δ is linearly ramped to the final value of $\delta = -2.1(3)E_r$, where the trivial band is expected in equilibrium (Fig. 4A). We first test the adiabaticity of the sweep process by probing the spin polarization for different sweep times, as shown in the inset of Fig. 4E. The value of the spin polarization at symmetric points is identical to the equilibrium case when the sweep time is longer than 5 ms. As a final

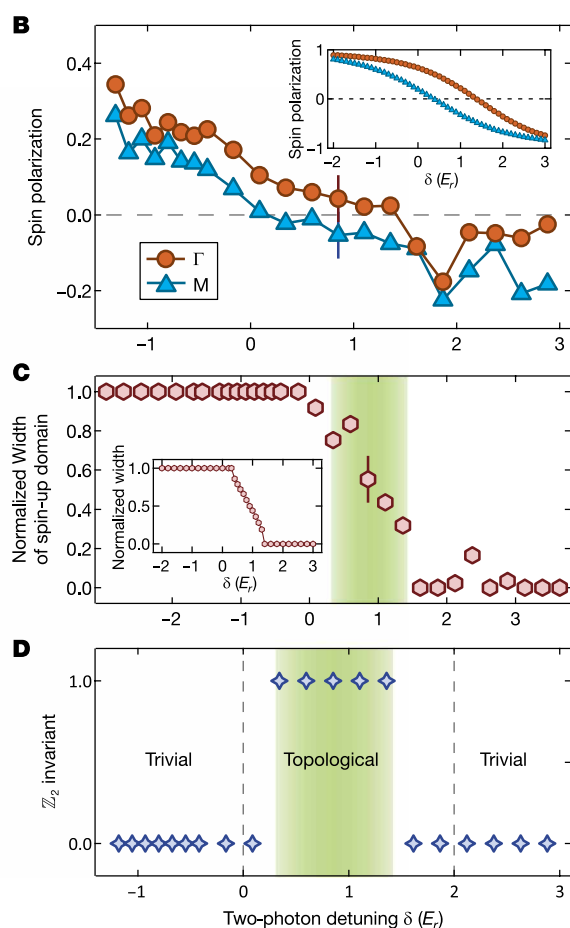
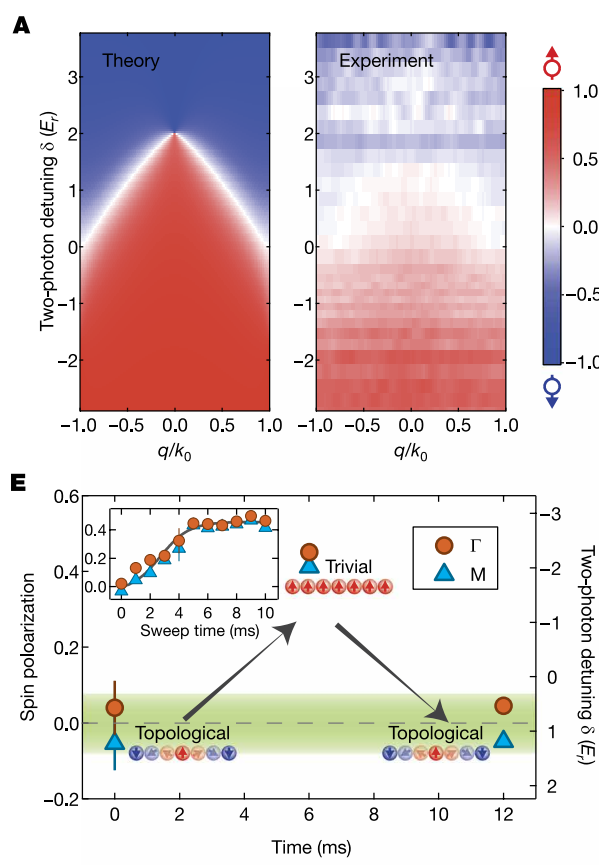


Fig. 4. In-equilibrium spin textures and their \mathbb{Z}_2 invariant across the topological transition. (A) Experimental measurement of spin polarization $P(q_x) = (n_\uparrow(q_x) - n_\downarrow(q_x)) / (n_\uparrow(q_x) + n_\downarrow(q_x))$ within FBZ as a function of two-photon detuning δ . For all measurements, the lattice depth and the Raman coupling strength are set to $V_\uparrow = 1.1(1)E_r$, $V_\downarrow = 4.2(4)E_r$, and $M_0 = 1.88(10)E_r$. Numerical calculation at $T = 0$ nK is shown for comparison. (B) The spin polarization is obtained at the symmetry points Γ and M . The inset figure gives numerical calculation based on experimental parameters. (C) Coexistence of $|\uparrow\rangle$ and $|\downarrow\rangle$ within the FBZ is visualized by measuring the width of the $|\uparrow\rangle$ domain of the spin texture normalized by $2\hbar k_0$ as a function of m_z . (D) The measured \mathbb{Z}_2 invariant v reveals the SPT band, which is consistent with the predicted region (shaded region) for the current experiment parameters. The vertical dashed line indicates the predicted phase transition point at $T = 0$ nK. (E) A topological band, adiabatically prepared at $\delta = 0.8(3)E_r$, initially, is converted into a trivial one at $\delta = -2.1(3)E_r$, and restored back to the original SPT band. The dashed line of the inset serves as a visual guide.

examination of the adiabatic control, we show that the SPT band can be converted into the trivial one and restored back to the topological one, as shown in Fig. 4E. The spin texture and its invariant measured at each time (0, 6, and 12 ms) are consistent with the equilibrium case.

Spin relaxation dynamics after quench

Having known the spin textures in equilibrium and their topological invariants, we now turn our attention to the far-from-equilibrium spin dynamics after the quench between the trivial and the topological regime. Using the dynamic control of the Hamiltonian, we particularly consider a bidirectional quench between the topological regime [$\delta = 0.8(3)E_r$] and the polarized spin- $|\uparrow\rangle$ trivial regime [$\delta = -2.1(3)E_r$] with the trap frequency $\omega_x = 2\pi \times 241(20)$ Hz and monitor the spin dynamics under the postquench Hamiltonian. Figure 5 shows experimental measurements of spin polarization at symmetric points after bidirectional quench, which reflects the topological nature of the postquench Hamiltonian. If the system is quenched to the topological regime with spin-orbit fields (Fig. 5A), then the q_x -dependent effective magnetic (spin-orbit) field leads to spin wave-like collective dynamics with spin relaxation to the final state. This is in sharp contrast to the case that the system is quenched to the trivial band where the spin is averagedly polarized to the z direction and the dominant spin dynamics show monotonous relaxation (Fig. 5B). It shows that the collective oscillation exhibits a frequency larger than the trapping frequency. This is because the trapping-induced intraband transition can experience an energy detuning between Bloch states at different momenta, which enhances the collective oscillation frequency (see the Supplementary Materials).

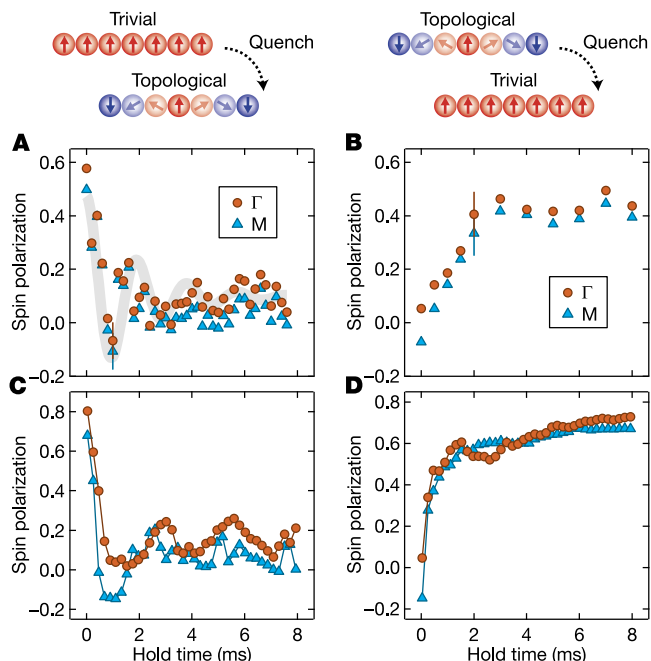


Fig. 5. Far-from-equilibrium spin dynamics after quench to SPT and trivial bands. (A and B) Measured spin dynamics after a quench from trivial to topological (A) or from topological to trivial (B). The parameters are $V_{\uparrow} = 1.1(1)E_r$, $V_{\downarrow} = 4.2(4)E_r$, and $M_0 = 1.88(10)E_r$. The two-photon detuning is set to be $\delta = -2.1(3)E_r$ and $0.8(3)E_r$ for the trivial and topological regime, respectively. The shaded region serves as a visual guide. (C and D) Numerical calculations of the quench dynamics. Parameters all take the same values as in (A) and (B), except $\delta = -1.5E_r$ ($\delta = 0.8E_r$) for the trivial (topological) regime. The temperature is set at $T = 150$ nK. The decay coefficient is taken as $\gamma = 0$ for (C) and $\gamma = 0.08$ for (D).

The observed topology-dependent spin dynamics show a quite very good agreement with numerical calculations taking into account the trap geometry, the finite temperature effect, and the dissipation process (Fig. 5, C and D). We emphasize that in the simulation of Fig. 5C, a vanishing decay coefficient has been chosen, while the simulation matches well with the experimental observations. This indicates that the spin dynamics in the quench to the topological regime are dominated by the trapping-induced intraband scatterings. We note that, although in general, the quench spin dynamics studied here may not be able to distinguish the phase close to the critical point of phase transition, the observed spin relaxation dynamics reflect the topological property of the band away from critical point after quench.

CONCLUSION

The novel SPT band we uncovered here highlights the great capabilities to realize and explore new topological physics with ultracold atoms. In particular, the study may open the way to observing all SPT phases of 1D in the AZ classification (9), including the chiral topological state of AIII class, which can be readily achieved by considering a spin-independent, rather than spin-dependent, optical lattice in Eq. 1 (16), the BDI and D classes of superfluids by adding attractive interactions (35), and also the exotic phases protected by nonsymmorphic symmetries (36, 37). Compared with the solid-state materials, whose complicated environment generally causes difficulty in engineering the symmetries, the full steerability of ultracold atoms can enable a precise study of broad classes of SPT phases, of which probing the reduction of topological classification of SPT phases from single particle to interacting regimes is a most fascinating topic has been extensively discussed in theory (9, 24, 38, 39). This important issue is very difficult to investigate in solid-state experiments because of the great challenges of realization but it is promising for ultracold atoms based on the current study with properly engineered interactions (16, 40).

Further generalization of the present study to higher dimensional systems also offers the simulation of quantum phases beyond natural conditions. For example, 2D tunable Dirac semimetals driven by spin-orbit coupling can be readily achieved by applying the present scheme to 2D systems (41) and are of particular interests because a spin-orbit-coupled 2D Dirac semimetal is still not available in solid-state materials (42). By tuning attractive interactions, the novel topological Fulde-Ferrell superfluid (43, 44) and Majorana zero modes protected by Chern-Simons invariant (45) have been predicted in these 2D Dirac semimetals. Finally, the nonequilibrium quench dynamics unveiled in this work show novel spin relaxation dynamics related to bulk topology. Generalization of the quench study to higher dimensional systems is expected to bring about more nontrivial quantum spin dynamics (46), which may provide insights into the understanding of nonequilibrium many-particle dynamics in the exotic phases.

MATERIALS AND METHODS

Experimental procedure

A degenerate equal mixture of $N_{\uparrow,\downarrow} = 5 \times 10^3$ ^{173}Yb atoms at $T/T_F = 0.4$ was prepared after forced-evaporative cooling in an ODT (28, 47), where T_F is the Fermi temperature of the trapped fermions with a trapping frequency of $\bar{\omega} = (\omega_x \omega_y \omega_z)^{1/3} = 2\pi \times 126$ Hz. A quantized axis was fixed by the bias magnetic field of 5 G applied along the \hat{z} direction. Before the two-photon Raman transition that couples $|\uparrow\rangle$ and $|\downarrow\rangle$ states was switched on, the intensity of the σ^- -polarized light (called a

lift beam) was linearly ramped up within 3 ms to lift the degeneracy of the ground levels. Simultaneously, we compensated the antitrapping effect of the blue-detuned light by increasing the depth of the dipole trap. A pair of Raman and lattice beams, with fixed two-photon detuning δ , was then exponentially ramped to the final value with the time constant of $\tau = 7$ ms, by which fermions were adiabatically loaded into the optical Raman lattice. Finally, the two-photon detuning δ (or equivalently m_z) was changed on demand, depending on the experiments. In the measurement of the topological invariant, the fermions were directly loaded into the Raman lattice with the fixed value of m_z . In the measurement of quench dynamics, two-photon detuning was suddenly switched from the initial ($\delta = 0.8E_r$, corresponding to the topological phase) to the final value ($\delta = -2.1E_r$, corresponding to the trivial phase) and vice versa (see fig. S5).

To obtain a TOF image sensitive to the spin state, we applied 556-nm blast pulses resonant to $^1S_0 \rightarrow ^3P_1(F' = 7/2)$ transition before the 6-ms TOF expansion. Using a 399-nm light resonant to $^1S_0 \rightarrow ^3P_1(F' = 7/2)$ transition with a blast pulse, three absorption images were obtained, providing a TOF atomic distribution \mathcal{I}_{m_F} after killing m_F -state atoms for 200 to 400 μ s. Finally, an atomic distribution of $m_F = 5/2$ and $m_F = 3/2$ atoms was extracted from $\mathcal{I}_{m_F=3/2} - \mathcal{I}_{m_F=5/2,3/2}$ and $\mathcal{I}_{m_F=5/2} - \mathcal{I}_{m_F=5/2,3/2}$, respectively. We integrated the whole atomic cloud along the k_z direction and obtained the atomic profile in the k_x momentum domain, as described in fig. S6.

SUPPLEMENTARY MATERIALS

Supplementary material for this article is available at <http://advances.sciencemag.org/cgi/content/full/4/2/eaao4748/DC1>

Supplementary Text

- fig. S1. Total spin polarizations of the lowest two bands at Γ and M points.
- fig. S2. Energy spectra of 1D Raman lattice Hamiltonian H , given by Eq. 1 in the main text, with open boundary condition, showing the existence of midgap end states.
- fig. S3. Quench dynamics under various conditions.
- fig. S4. Electronic hyperfine level of ^{173}Yb atoms and Raman coupling.
- fig. S5. Experimental sequences.
- fig. S6. Spin-sensitive TOF images.

REFERENCES AND NOTES

1. K. v. Klitzing, G. Dorda, M. Pepper, New method for high-accuracy determination of the fine-structure constant based on quantized Hall resistance. *Phys. Rev. Lett.* **45**, 494–497 (1980).
2. D. C. Tsui, H. L. Stormer, A. C. Gossard, Two-dimensional magnetotransport in the extreme quantum limit. *Phys. Rev. Lett.* **48**, 1559–1562 (1982).
3. X.-G. Wen, Topological orders in rigid states. *Int. J. Mod. Phys. B* **4**, 239–271 (1990).
4. A. Kitaev, J. Preskill, Topological entanglement entropy. *Phys. Rev. Lett.* **96**, 110404 (2006).
5. M. Levin, X.-G. Wen, Detecting topological order in a ground state wave function. *Phys. Rev. Lett.* **96**, 110405 (2006).
6. X. Chen, Z.-C. Gu, X.-G. Wen, Local unitary transformation, long-range quantum entanglement, wave function renormalization, and topological order. *Phys. Rev. B* **82**, 155138 (2010).
7. A. P. Schnyder, S. Ryu, A. Furusaki, A. W. W. Ludwig, Classification of topological insulators and superconductors in three spatial dimensions. *Phys. Rev. B* **78**, 195125 (2008).
8. A. Kitaev, *AIP Conference Proceedings* (AIP, 2009), vol. 1134, pp. 22–30.
9. S. Ryu, A. P. Schnyder, A. Furusaki, A. W. W. Ludwig, Topological insulators and superconductors: Tenfold way and dimensional hierarchy. *New J. Phys.* **12**, 065010 (2010).
10. X. Chen, Z.-C. Gu, Z.-X. Liu, X.-G. Wen, Symmetry-protected topological orders in interacting bosonic systems. *Science* **338**, 1604–1606 (2012).
11. W. P. Su, J. R. Schrieffer, A. J. Heeger, Solitons in polyacetylene. *Phys. Rev. Lett.* **42**, 1698–1701 (1979).
12. F. D. M. Haldane, Continuum dynamics of the 1-D Heisenberg antiferromagnet: Identification with the O(3) nonlinear sigma model. *Phys. Lett. A* **93**, 464–468 (1983).
13. M. Z. Hasan, C. L. Kane, *Colloquium: Topological insulators*. *Rev. Mod. Phys.* **82**, 3045–3067 (2010).
14. X.-L. Qi, S.-C. Zhang, Topological insulators and superconductors. *Rev. Mod. Phys.* **83**, 1057–1110 (2011).
15. C.-K. Chiu, J. C. Y. Teo, A. P. Schnyder, S. Ryu, Classification of topological quantum matter with symmetries. *Rev. Mod. Phys.* **88**, 035005 (2016).
16. X.-J. Liu, Z.-X. Liu, M. Cheng, Manipulating topological edge spins in a one-dimensional optical lattice. *Phys. Rev. Lett.* **110**, 076401 (2013).
17. H. Nonne, M. Moliner, S. Capponi, P. Lecheminant, K. Totsuka, Symmetry-protected topological phases of alkaline-earth cold fermionic atoms in one dimension. *Europhys. Lett.* **102**, 37008 (2013).
18. L. Lu, C. Fang, L. Fu, S. G. Johnson, J. D. Joannopoulos, M. Soljacic, Symmetry-protected topological photonic crystal in three dimensions. *Nat. Phys.* **12**, 337–340 (2016).
19. M. Atala, M. Aidelsburger, M. Lohse, J. T. Barreiro, B. Paredes, I. Bloch, Observation of chiral currents with ultracold atoms in bosonic ladders. *Nat. Phys.* **10**, 588–593 (2014).
20. E. J. Meier, F. A. An, B. Gadway, Observation of the topological soliton state in the Su-Schrieffer-Heeger model. *Nat. Commun.* **7**, 13986 (2016).
21. M. Leder, C. Grossert, L. Sitta, M. Genske, A. Rosch, M. Weitz, Real-space imaging of a topologically protected edge state with ultracold atoms in an amplitude-chirped optical lattice. *Nat. Commun.* **7**, 13112 (2016).
22. A. Altland, M. R. Zirnbauer, Nonstandard symmetry classes in mesoscopic normal-superconducting hybrid structures. *Phys. Rev. B* **55**, 1142–1161 (1997).
23. X.-J. Liu, K. T. Law, T. K. Ng, P. A. Lee, Detecting topological phases in cold atoms. *Phys. Rev. Lett.* **111**, 120402 (2013).
24. L. Fidkowski, A. Kitaev, Topological phases of fermions in one dimension. *Phys. Rev. B* **83**, 075103 (2011).
25. G. Lindblad, On the generators of quantum dynamical semigroups. *Commun. Math. Phys.* **48**, 119–130 (1976).
26. Y. Hu, P. Zoller, J. C. Budich, Dynamical buildup of a quantized Hall response from nontopological states. *Phys. Rev. Lett.* **117**, 126803 (2016).
27. Z. Wu, L. Zhang, W. Sun, X.-T. Xu, B.-Z. Wang, S.-C. Ji, Y. Deng, S. Chen, X.-J. Liu, J.-W. Pan, Realization of two-dimensional spin-orbit coupling for Bose-Einstein condensates. *Science* **354**, 83–88 (2016).
28. B. Song, C. He, S. Zhang, E. Hajiyev, W. Huang, X.-J. Liu, G.-B. Jo, Spin-orbit-coupled two-electron Fermi gases of ytterbium atoms. *Phys. Rev. A* **94**, 061604 (2016).
29. Y.-J. Lin, K. Jiménez-García, I. B. Spielman, Spin-orbit-coupled Bose-Einstein condensate. *Nature* **471**, 83–86 (2011).
30. P. Wang, Z.-Q. Yu, Z. Fu, J. Miao, L. Huang, S. Chai, H. Zhai, J. Zhang, Spin-orbit coupled degenerate Fermi gases. *Phys. Rev. Lett.* **109**, 095301 (2012).
31. L. W. Cheuk, A. T. Sommer, Z. Hadzibabic, T. Yefsah, W. S. Bakr, M. W. Zwierlein, Spin-injection spectroscopy of a spin-orbit coupled Fermi gas. *Phys. Rev. Lett.* **109**, 095302 (2012).
32. N. Q. Burdick, Y. Tang, B. L. Lev, Long-lived spin-orbit-coupled degenerate dipolar Fermi gas. *Phys. Rev. X* **6**, 031022 (2016).
33. M. Mancini, G. Pagano, G. Cappellini, L. Livi, M. Rider, J. Catani, C. Sias, P. Zoller, M. Inguscio, M. Dalmonte, L. Fallani, Observation of chiral edge states with neutral fermions in synthetic Hall ribbons. *Science* **349**, 1510–1513 (2015).
34. J. Li, W. Huang, B. Shteynas, S. Burchesky, F. Top, E. Su, J. Lee, A. O. Jamison, W. Ketterle, Spin-orbit coupling and spin textures in optical superlattices. *Phys. Rev. Lett.* **117**, 185301 (2016).
35. J. J. He, J. Wu, T.-P. Choy, X.-J. Liu, Y. Tanaka, K. T. Law, Correlated spin currents generated by resonant-crossed Andreev reflections in topological superconductors. *Nat. Commun.* **5**, 3232 (2014).
36. H. Chen, X.-J. Liu, X. C. Xie, Hidden nonsymmorphic symmetry in optical lattices with one-dimensional spin-orbit coupling. *Phys. Rev. A* **93**, 053610 (2016).
37. S.-L. Zhang, Q. Zhou, Two-leg Su-Schrieffer-Heeger chain with glide reflection symmetry. *Phys. Rev. A* **95**, 061601 (2016).
38. Z.-C. Gu, M. Levin, Effect of interactions on two-dimensional fermionic symmetry-protected topological phases with Z_2 symmetry. *Phys. Rev. B* **89**, 201113 (2014).
39. T. Morimoto, A. Furusaki, C. Mudry, Breakdown of the topological classification \mathbb{Z} for gapped phases of noninteracting fermions by quartic interactions. *Phys. Rev. B* **92**, 125104 (2015).
40. X. Zhou, J.-S. Pan, Z.-X. Liu, W. Zhang, W. Yi, G. Chen, S. Jia, Symmetry-protected topological states for interacting fermions in alkaline-earth-like atoms. *Phys. Rev. Lett.* **119**, 185701 (2017).
41. T. F. J. Poon, X.-J. Liu, From a semimetal to a chiral Fulde-Ferrell superfluid. *Phys. Rev. B* **97**, 020501 (2018).
42. S. M. Young, C. L. Kane, Dirac semimetals in two dimensions. *Phys. Rev. Lett.* **115**, 126803 (2015).
43. C. Qu, Z. Zheng, M. Gong, Y. Xu, L. Mao, X. Zou, G. Guo, C. Zhang, Topological superfluids with finite-momentum pairing and Majorana fermions. *Nat. Commun.* **4**, 2710 (2013).
44. W. Zhang, W. Yi, Topological Fulde-Ferrell-Larkin-Ovchinnikov states in spin-orbit-coupled Fermi gases. *Nat. Commun.* **4**, 2711 (2013).

45. C. Chan, L. Zhang, T. F. J. Poon, Y.-P. He, Y.-Q. Wang, X.-J. Liu, Generic theory for Majorana zero modes in 2D superconductors. *Phys. Rev. Lett.* **119**, 047001 (2017).
46. C. Wang, P. Zhang, X. Chen, J. Yu, H. Zhai, Scheme to measure the topological number of a chern insulator from quench dynamics. *Phys. Rev. Lett.* **118**, 185701 (2017).
47. B. Song, Y. Zou, S. Zhang, C.-w. Cho, G.-B. Jo, A cost-effective high-flux source of cold ytterbium atoms. *Appl. Phys. B* **122**, 250 (2016).

Acknowledgments: We thank T.-L. Ho, Q. Zhou, K. T. Law, S. Z. Zhang, and C.-K. Chan for the useful discussion. We also thank Y. Zou, W. Huang, and G. Cai for the experimental assistance. **Funding:** G.-B.J. acknowledges the support from the Hong Kong Research Grants Council and the Croucher Foundation through ECS26300014, GRF16300215, GRF16311516, GRF16305317, and the Croucher Innovation grants. X.-J.L. acknowledges the support from the National Key R&D Program of China (under grant 2016YFA030160X), the NSFC (nos. 11574008 and 11761161003), and the Thousand-Young-Talent Program of China. **Author contributions:** B.S., C.H., E.H., and S.Z. carried out the experiment, data analysis, and the

numerical calculation. L.Z. and T.F.J.P. performed the theoretical modeling and the numerical calculations. All authors discussed the results and commented on the manuscript. G.-B.J. and X.-J.L. supervised the research. **Competing interests:** The authors declare that they have no competing interests. **Data and materials availability:** All data needed to evaluate the conclusions in the paper are present in the paper and/or the Supplementary Materials. Additional data related to this paper may be requested from the authors.

Submitted 25 July 2017

Accepted 23 January 2018

Published 23 February 2018

10.1126/sciadv.aao4748

Citation: B. Song, L. Zhang, C. He, T. F. J. Poon, E. Hajiyev, S. Zhang, X.-J. Liu, G.-B. Jo, Observation of symmetry-protected topological band with ultracold fermions. *Sci. Adv.* **4**, eao4748 (2018).

Science Advances

Observation of symmetry-protected topological band with ultracold fermions

Bo Song, Long Zhang, Chengdong He, Ting Fung Jeffrey Poon, Elnur Hajiiev, Shanchao Zhang, Xiong-Jun Liu and Gyu-Boong Jo

Sci Adv 4 (2), eaao4748.
DOI: 10.1126/sciadv.aao4748

ARTICLE TOOLS

<http://advances.sciencemag.org/content/4/2/eaao4748>

SUPPLEMENTARY MATERIALS

<http://advances.sciencemag.org/content/suppl/2018/02/16/4.2.eaao4748.DC1>

REFERENCES

This article cites 46 articles, 3 of which you can access for free
<http://advances.sciencemag.org/content/4/2/eaao4748#BIBL>

PERMISSIONS

<http://www.sciencemag.org/help/reprints-and-permissions>

Use of this article is subject to the [Terms of Service](#)

Science Advances (ISSN 2375-2548) is published by the American Association for the Advancement of Science, 1200 New York Avenue NW, Washington, DC 20005. 2017 © The Authors, some rights reserved; exclusive licensee American Association for the Advancement of Science. No claim to original U.S. Government Works. The title *Science Advances* is a registered trademark of AAAS.